Ab Initio and Density-Functional Calculations of the Vibrational Structure of the Singlet and Triplet Excited States of Pyrazine

Peter Weber and Jeffrey R. Reimers*

School of Chemistry, University of Sydney, Sydney, New South Wales 2006, Australia

Received: April 28, 1999; In Final Form: September 16, 1999

We evaluate using a range of ab initio and density-functional approaches the vibrational frequencies, including correction for diagonal anharmonicity, of the lowest triplet state of pyrazine $T_1(^3B_{3u})$; less extensive calculations are also performed for the ground state, three excited singlet states, and five other triplet states. The results indicate that CASSCF-based methods are cumbersome to apply to molecules of this size, with no practicable CASSCF methodology producing a continuous potential energy surface for T_1. While CASPT2 (and also MRCI) methods can correct for erroneous CASSCF state energies, they are not capable of removing the effects of erroneous CASSCF conical intersections. Density-functional schemes, and in particular B3LYP, provide the best qualitative and quantitative results, with the time-dependent approximation to density-functional theory providing results comparable with those from direct evaluation. An overview of vibronic coupling theory is presented and used to demonstrate the relative strengths and weaknesses of these Born−Oppenheimer calculations compared to the traditional diabatic vibronic coupling calculations of Fischer. In particular, for $T_1(^3B_{3u})$, the current assignments of the strongly vibronically active modes ν_4, ν_5, and ν_{10a} are readily verified, vibronic activity is predicted for ν_{12}, the anomalous behavior of ν_{16a} and ν_{16b} is reproduced, and ν_{8a} is reassigned.

I. Introduction

The electronic structures of the azabenzenes have been studied extensively using a range of experimental techniques,[1] and as a result, these molecules have often been used for the verification of new computational schemes.[2−14] A range of interesting and complex properties such as vibronic coupling are displayed,[15] with, e.g., the S_1 and S_2 states of pyrazine forming a conical intersection within the Franck−Condon region.[11] Nevertheless, no complete experimentally based vibrational analysis for any excited state of any azine is yet available, and many observed features remain unexplained; for pyrazine, e.g., only half of the 24 vibrational modes have been assigned for the S_1 and T_1 excited states.[1,16,17] One of the most important results to come from the study of azines has been the verification[1,15,18,19] of the through-bond electronic-coupling mechanism of Hoffman.[20,21] This describes the interaction of lone-pair electrons on different nitrogen atoms within the azine as arising from both short-range through-space overlap interactions and long-range through-bond superexchange interactions. Experimental manifestations of this include the relative ordering and point-group symmetry of different (n,π^*) excited states. Consider, for example, the diazines pyrazine, pyrimidine, and pyridazine. If a lone-pair electron is removed from a nitrogen atom, its CNC bond angle expands and the resulting energy lowering is known as the *reorganization energy*. Two possibilities arise for such a transition in a diazine, however: removal of an electron from one nitrogen, or removal of density corresponding to half of an electron from each nitrogen. The reorganization energy is much larger in the former case and tends to localize (or trap) the (n,π^*) excitation on just one of the two nitrogens, reducing the point-group symmetry of the excited state. In competition with this effect is the inter-lone-pair coupling which tends to delocalize (or share) the excitation equally over both nitrogens, preferring high symmetry. Because of the effects of through-bond coupling, in each diazine the electronic coupling is dominant and high-symmetry results.[22−24] Actually, this type of problem is very general, forming, for example, the key questions[25] concerning the electronic properties of the famous Creutz−Taube ion[26] [Ru(NH$_3$)$_5$−pyrazine−Ru(NH$_3$)$_5$]$^{5+}$ and the special-pair radical cation whose properties are central to biological photosynthesis. In problems of this type, the principal issues involve (1) determining the identity and energy of the low-lying excited states and (2) determining whether the excited state has a single minimum (all vibration frequencies at the high-symmetry geometry are real) or a double minimum (an imaginary frequency at the high-symmetry geometry). Central to this is the determination of the strength of the vibronic coupling acting between localized diabatic electronic states of the molecule.

For many azines, the identities of a variety of low-lying excited states are now known. We have reviewed this literature in a companion paper;[27] here, we consider issue 2 only.

Vibrational analyses of excited states are much more difficult to obtain than those of ground states. Experimentally, typically only the lowest singlet and triplet excited states can be observed in sufficient resolution to identify individual vibrational transitions, and vibronic coupling or Duschinsky rotation effects make the assignment of these transitions difficult. Computationally, the mapping of excited-state adiabatic potential energy surfaces is complicated by possible instabilities in the Hartree−Fock or Kohn−Sham solutions.[28] One such instability for the S_1 state of pyrazine is well-known[4−6] and results in a much lower self-consistent field (SCF) energy being determined for this state at D_{2h} nuclear geometries when the electronic wave function is allowed to relax to one of C_{2v} symmetry. Vibrations of b_{1u} symmetry distort the nuclear geometry in an analogous fashion, and hence, when the S_1 potential energy surface is examined as a function of any b_{1u} normal mode (say ν_{12}), it is discontinuous. A continuous potential energy surface can be established

* To whom correspondence should be addressed.

10.1021/jp991404k CCC: $18.00
Published on Web 11/12/1999

TABLE 1: Description of the State Averaging and Orbital Spaces Used in CASSCF and CASPT2 Calculations[a]

		size	doubly occupied								active space							
calculation	optimized energy	(*n*,*m*)	a_g	b_{3u}	b_{2u}	b_{1g}	b_{1u}	b_{2g}	b_{3g}	a_u	a_g	b_{3u}	b_{2u}	b_{1g}	b_{1u}	b_{2g}	b_{3g}	a_u
analytical	$T_1(^3B_{3u})$	(10,8)	5	0	4	0	4	0	3	0	1	2	0	1	1	2	0	1
a_g: $\nu_{1,6a,8a,9a}$	$T_1(^3B_{3u})$	(12,9)	5	0	4	0	4	0	2	0	1	2	0	1	1	2	1	1
b_{2g}: $\nu_{4,5}$	$T_1(^3B_{3u}) + T_2(^3B_{1u})$	(12,10)	5	0	4	0	4	0	2	0	3	2	0	1	1	1	1	1
b_{1g}: ν_{10a}	$T_1(^3B_{3u})$	(12,10)	5	0	4	0	4	0	2	0	1	2	0	1	1	2	2	1
b_{1u}: ν_{12}	$T_1(^3B_{3u}) + T_5(^3B_{2g})$	(10,8)	5	0	4	0	4	0	3	0	1	2	0	1	1	2	0	1
a_u: ν_{16a}	$T_1(^3B_{3u})$	(12,10)	5	0	4	0	4	0	2	0	1	2	1	1	1	2	1	1
b_{3u}: ν_{16b}	$T_1(^3B_{3u})$	(12,10)	5	0	4	0	4	0	2	0	1	2	0	1	2	2	1	1

[a] Different orbital spaces and state averages are used for the analytical frequency calculation and for the single-point energy calculations along normal modes of different symmetry types. The size is specified by *n*, the number of active electrons, and *m*, the number of active orbitals in which these electrons are distributed.

by using multiconfigurational wave functions such as valence-bond wave functions[4,6] or state-averaged complete-active-space SCF (CASSCF) wave functions,[23] with (typically) a double-well potential resulting. Dynamic electron correlation favors high-symmetry configurations, however, and after a multireference configuration-interaction (MRCI) calculation based on the CASSCF wave function, a single-well potential is obtained, as is observed experimentally.[23] Hence, the level of theory, and the level of caution, necessary to satisfactorily complete an excited-state vibrational analysis is appreciable.

In this work we consider primarily the vibrational structure of the lowest triplet state of pyrazine, $T_1(^3B_{3u})$. For this state, 8 of the 24 vibrational frequencies have been experimentally assigned by Fischer,[17] and various other possible vibration frequencies have been suggested;[29,30] we concentrate on the theoretical prediction of the eight assigned frequencies. Note that this state is selected for detailed study in preference to S_1-($^1B_{3u}$) as we can apply a larger range of theoretical techniques to the triplet state,[27] and as much is already known[11] about S_1 and its low-lying conical intersection with $S_2(^1B_{2u})$.

We perform both harmonic and anharmonic analyses within the Born−Oppenheimer approximation, but do not consider vibronic coupling beyond this level. Vibronic coupling usually lowers the vibration frequency, and calculations which fully include this effect are very difficult to perform quantitatively a priori. Born−Oppenheimer vibrational analyses form but the first step in this procedure, accounting for some but not all effects of vibronic coupling; progress beyond this level requires the identification of all states involved and the evaluation and processing of nonadiabatic-coupling matrix elements.

In addition to this study of $T_1(^3B_{3u})$, we consider briefly harmonic analyses of the vibrational properties of the ground state $S_0(^1A_g)$ and the excited states $S_1(^1B_{3u})$, $S_2(^1B_{2u})$, $S_3(^1A_u)$, $T_2(^3B_{1u})$, $T_3(^3A_u)$, $T_4(^3B_{2u})$, $T_5(^3B_{2g})$, and $T_6(^3B_{1u})$. The notation used for these states is described in detail elsewhere.[27] A full description of the results, including optimized energies, Cartesian coordinates, normal modes, normal-mode displacements and reorganization energies from the ground state, and Duschinsky matrixes, obtained using up to five electronic structure methods, is given in full in the Supporting Information.

II. Electronic Structure Computational Methods

A total of eight different ab initio and density-functional computational schemes are employed to determine vibrational properties of the excited states of pyrazine. These methods have been described in full elsewhere,[27] but briefly they are termed SVWN, SVWN-TDDFT, B3LYP, B3LYP-TDDFT, CIS, CASSCF, MP2, and CASPT2. For the direct density-functional-theory (DFT) methods SVWN (local density functional[31,32]) and B3LYP (a hybrid functional with exact exchange[33]), the GAUSSIAN-94 program is used.[34] Their variants SVWN-TDDFT and B3LYP-TDDFT involve the use of time-dependent perturbation theory[13,35] to determine excited-state energies using TURBOMOLE.[36] For pyrazine, we have shown that the triplet vertical excitation energies predicted by this TDDFT scheme are similar to those evaluated directly, and also that, for both singlet and triplet states, the B3LYP-TDDFT energies are equivalent in accuracy to those[7,14,27,37] from the most accurate ab initio methods, CASPT2 and EOM-CCSD(T). A variety of DFT methods for excited states are becoming available; we have reviewed this literature and explicitly considered a range of these methods in the companion paper.[27] Of the ab initio methods, the CIS[38] and MP2[39] calculations are performed using GAUSSIAN-94,[34] the CASSCF and CASPT2[40] energies are evaluated using MOLCAS,[41] and the CASSCF analytical frequencies are evaluated using DALTON;[42] some multirepresentation state-average calculations are performed using MOLPRO.[43] The active spaces used in the CASSCF and CASPT2 calculations are given in Table 1 and described in detail later in section IV.B; these are described as (*n*,*m*) where *n* is the number of electrons distributed in *m* orbitals. All calculations are performed using the cc-pVDZ basis set.[44]

III. Ground State $S_0(^1A_g)$

Results from a variety of calculations of the normal modes of pyrazine S_0 are available in the literature, obtained using both density-functional[12,45] and ab initio[11,45] methods with basis sets comparable to or larger than cc-pVDZ. To aid in our analysis of the excited-state vibrations, we have performed vibrational analyses of the ground state using the SCF, SVWN, B3LYP, MP2, and CASSCF(10,8) methods. We present in Tables 2 and 3 only brief summaries of the results obtained, but all results are given in the Supporting Information. Table 2 shows the maximum error found between calculated and gas-phase experimental frequencies for all 24 modes and the associated root-mean-square (RMS) error. Also, for each method, a multiplicative scale factor is optimized to minimize the RMS errors, and the maximum and RMS errors for the scaled vibration frequencies are also given in the table; the calculated scale factors for SCF, SVWN, B3LYP, MP2, and CASSCF are 0.90, 0.99, 0.97, 0.96, and 0.92, respectively. The results are quite good, with the RMS error after scaling ranging between 20 and 43 cm^{-1}, while the largest error found is just 170 cm^{-1}.

Table 3 provides a summary of the Duschinsky rotation matrixes which map the normal coordinates obtained from the SCF, SVWN, B3LYP, and MP2 methods onto those from CASSCF. In general, these modes map smoothly, with the *i*th mode of a particular symmetry having the same shape for all methods. However, one exception appears within the b_{2u} vibrations: the relative order of ν_{14} and ν_{18b} differs between the SCF and CASSCF methods and those that include dynamic electron correlation: MP2, SVWN, and B3LYP. Disagreement

TABLE 2: Statistical Comparison of the Maximum and RMS Differences, cm^{-1}, between Observed and Calculated Vibration Frequencies[a]

el str method	state	vibr method	raw, all data		scaled, all data		ν_1, ν_{6a}, ν_{9a}, ν_{16a}, ν_{16b} unscaled	
			max	RMS	max	RMS	max	RMS
B3LYP	S_0	AN	137	56	53	20	29	17
B3LYP	T_1	AN	338	173	335	158	43	35
B3LYP	T_1	NUM	343	126	292	106	49	30
B3LYP-TDDFT	T_1	NUM	353	135	302	117	51	32
B3LYP	T_1	ANH	328	131	278	110	40	31
B3LYP-TDDFT	T_1	ANH	342	137	291	117	39	31
SVWN	S_0	AN	184	47	170	43	27	25
SVWN	T_1	AN	340	147	323	140	53	28
SVWN	T_1	NUM	311	132	294	126	40	29
SVWN-TDDFT	T_1	NUM	316	148	299	143	43	34
SVWN	T_1	ANH	289	132	273	126	52	31
SVWN-TDDFT	T_1	ANH	294	134	278	129	50	32
SCF	S_0	AN	332	170	72	30	112	89
CIS	T_1	AN	697	332	602	260	135	97
CASSCF	S_0	AN	336	150	93	38	89	63
CASSCF	T_1	AN	429	179	290	117	117	73
CASSCF	T_1	NUM	934	369	831	312	117	76
CASSCF	T_1	ANH	796	338	705	281	121	80
MP2	S_0	AN	211	86	150	43	21	12
UMP2	T_1	AN	965	387	908	358	48	36
CASPT2	T_1	NUM	383	150	310	123	65	41
CASPT2	T_1	ANH	353	146	281	118	52	30

[a] For $S_0(^1A_g)$, "all data" includes all 24 modes, while for $T_1(^3B_{3u})$ it involves only 8, ν_1, ν_4, ν_{6a}, ν_{8a}, ν_{9a}, ν_{10a}, ν_{16a}, and ν_{16b}. AN (analytical) frequencies are from analytical second-derivative calculations, while NUM (numerical harmonic) and ANH (numerical anharmonic) frequencies are from analysis of the potential surfaces along the appropriate CASSCF analytical normal modes.

for these modes is not unexpected as the observed frequencies differ by only 86 cm^{-1}; experimental evidence distinguishing between the two possibilities is not currently available.

IV. Excited States

A. Overview of the Results for $T_1(^3B_{3u})$. For this state, analytical harmonic vibration frequencies have been evaluated using CIS, CASSCF(10,8), UMP2, SVWN, and B3LYP. A summary of the differences between the eight experimentally assigned[17] frequencies (ν_1, ν_4, ν_{6a}, ν_{8a}, ν_{9a}, ν_{10a}, ν_{16a}, and ν_{16b}) and the corresponding calculated ones is given in Table 2, while the frequencies themselves are given in Table 4 and the Duschinsky matrixes depicting rotations between the ground- and excited-state normal coordinates are summarized in Table 3; in the Supporting Information are given in full all of the optimized geometries, calculated vibration frequencies, normal modes, and Duschinsky matrixes. Results are also given in Table 4 for two other modes, ν_5 and ν_{12}, for which no firm assignment has been suggested but for which considerable interest exists, while results for all non-CH infrared-active modes are given later in Table 5.

To facilitate discussion, Figure 1 shows the form of each of the 10 normal modes considered in detail, as well as the change in potential energy evaluated using B3LYP, B3LYP-TDDFT, CASSCF, and CASPT2 when pyrazine is distorted along each mode. The CASSCF geometry and normal modes for $^3B_{3u}$ are used, and the displacement is given in terms of the zero-point displacement Q_{zpt} for each mode (in the harmonic approximation, the energy increase at displacement $Q = Q_{zpt}$ is $h\nu/2$). Vibration frequencies obtained using both harmonic and anharmonic analyses of these curves are given in Table 4, and statistical analyses of the results are given in Table 1. Finally, Figures 2 and 3 show additional energy surfaces obtained for distortion along ν_{12} and ν_4, respectively.

From Table 2 it is clear that the agreement between the observed and calculated frequencies is much poorer than that found for the ground-state vibrations, the maximum and RMS errors being typically 2−4 times larger. Also, as shown in the table, application of the ground-state scaling factors does not significantly improve the agreement. Possible causes of this include poor applicability of the computational schemes to excited states, incorrect representation of the nuclear-coordinate dependence of interstate couplings, neglect of nonadiabatic coupling, and possibly also incorrect experimental assignments. The first two issues are clearly the most important ones: a priori computations cannot address issues of nonadiabatic coupling and experimental assignments unless the electronic structure methods produce high-quality Born−Oppenheimer potential energy surfaces.

First we note in Table 4 that, of the eight modes, relatively good agreement is found for five: the totally symmetric modes ν_{6a}, ν_1, and ν_{9a} as well as ν_{16a} (a_u) and ν_{16b} (b_{3u}). The other totally symmetric mode ν_{8a} appears consistently overestimated by ca. 300−400 cm^{-1}, while ν_{10a} and ν_4 are, in general, very poorly reproduced. The maximum and RMS errors for both the ground and excited states obtained from just the above-mentioned first five modes are also given in Table 2. For the ground state, these results are significantly better than those obtained through the consideration of all modes; for the excited state, the errors are larger than those for the ground state but remain small, with RMS errors being on the order of 40 cm^{-1}. Hence, we conclude that, in principle, the computational methods are capable of quantitatively describing the excited-state vibrations.

The quality of the agreement found for ν_{6a}, ν_1, and ν_{9a} suggests that the computational schemes are correctly representing any coordinate dependence of the interaction between various $^3B_{3u}$ excited states, and it appears acceptable to ignore nonadiabatic coupling involving the a_g modes. Hence, the systematic overestimation of ν_{8a} must either arise from some highly mode specific interaction or be indicative of an incorrect experimental assignment. This issue is specifically addressed later in the Conclusions.

TABLE 3: Summary of Symmetry Blocks of Duschinsky Matrixes[a]

method	state	a_g	b_{1u}	b_{2u}	b_{3g}	a_u	b_{1g}	b_{2g}	b_{3u}
CASSCF	$S_1(^1B_{3u})$		D	S	S		i	D	
CASSCF	$S_2(^1B_{3u})$		M	S				D	
CASSCF	$S_3(^1A_u)$		i	S	Si			S	
CASSCF	$T_1(^3B_{3u})$		D	S	S			Di	
CASSCF	$T_2(^3B_{1u})$			S	Si			D	
CASSCF	$T_3(^3A_u)$		i	S					S
CASSCF	$T_4(^3B_{2u})$		d	Sd					
CASSCF	$T_5(^3B_{2g})$		D	S	S				
CASSCF	$T_6(^3B_{1u})$		S	S					
SCF	$S_0(^1A_g)$								
CIS	$S_1(^1B_{3u})$		M	M	S				
CIS	$S_3(A_u)$			S	Si		i		M
CIS	$T_1(^3B_{3u})$		Mi	S			i	S	
CIS	$T_2(^3B_{1u})$			S	Si				
CIS	$T_3(^3A_u)$			S					M
CIS	$T_4(^3B_{2u})$			S			i		
CIS	$T_5(^3B_{2g})$		S			i			
CIS	$T_6(^3B_{1u})$		M	Mi					i
MP2	$S_0(^1A_g)$			S					
UMP2	$T_1(^3B_{3u})$		D	S			D	D	
SVWN	$S_0(^1A_g)$			S					
SVWN	$T_1(^3B_{3u})$			S	S				
B3LYP	$S_0(^1A_g)$			S					
B3LYP	$T_1(^3B_{3u})$			S	S		i		
B3LYP	$T_2(^3B_{1u})$		S	S	Si			S	i
B3LYP	$T_3(^3A_u)$			S	Si		i	S	S
B3LYP	$T_4(^3B_{2u})$			S	S				
B3LYP	$T_5(^3B_{2g})$		S	S	S				i
B3LYP	$T_6(^3B_{1u})$			S	Si	i	i	M	

[a] Ground-state Duschinsky matrixes are the rotations with respect to the CASSCF ground-state normal coordinates, while excited-state Duschinsky matrixes are with respect to the ground-state normal coordinates determined by the most analogous method. Full results are given in the Supporting Information. The flag "i" indicates that one harmonic frequency is imaginary (but does not indicate whether or not the double-well potential can support localized zero-point vibration), "S" indicates that normal modes have interchanged in order within the symmetry block, "M" indicates strong normal mode mixing, "D" indicates that the potential-energy surface is known to be discontinuous for displacements of that type, and "d" indicates suspected discontinuous, and no flag indicates that the normal modes are similar. For the in-plane symmetries a_g, b_{1u}, b_{2u}, and b_{3g} there are five, four, four, and four modes, respectively, while for the out-of-plane symmetries a_u, b_{1g}, b_{2g}, and b_{3u} there are two, one, two, and two modes, respectively. Note that the pattern obtained for perdeuteropyrazine is significantly different from this.

Experimentally,[17] the vibrational modes involved in the strongest vibronic coupling are ν_{10a} and ν_4, and it is for these modes that the largest errors between calculated and observed frequencies occur. Before proceeding, we examine in section C vibronic coupling and the various approaches used to treat it. First, however, we note that, in Table 4, a selection of the UMP2 and CASSCF frequencies are clearly absurd, e.g., UMP2, $\nu_{10a} = 22\,042$ cm^{-1}! This is associated with *wave function instability*.

B. Wave Function Instability. For $S_1(^1B_{3u})$, it is well-known[4-6] that (spin-adapted) single-determinant SCF wave functions are unstable, with wave functions of C_{2v} symmetry having lower energy than corresponding ones of D_{2h} symmetry. The physical reason for this is that, in C_{2v} symmetry, the (n,π*) excitation localizes on one of the two nitrogens rather than delocalizing over both, as is required in D_{2h}; lone-pair localized single determinants have lower energy than delocalized ones. Distortions of pyrazine by modes of b_{1u} symmetry, e.g., ν_{12}, reduce the nuclear symmetry from D_{2h} to C_{2v}. In particular, ν_{12} has the effect of enlargening the CNC bond angle about the nitrogen on which the excitation is localized, favoring localization, and thus the energy of localized determinants decreases. The simplest method by which a continuous potential energy surface can be constructed is through use of two nonorthogonal determinants in a valence-bond type computation.[4,6] In principle, CASSCF can also produce a continuous potential energy surface through the inclusion of both lone-pair orbitals and the π* orbital in the active space. The active space (10,8) which we employ fulfills this criterion; it contains the two lone-pair orbitals and all six valence π orbitals. However, a small discontinuity remains in the CASSCF(10,8) potential energy surface, this arising as the lone pairs are mixed with other σ orbitals, and these must also be included in the active space.

The triplet state $T_1(^3B_{3u})$ behaves in a fashion directly analogous to $S_1(^1B_{3u})$, and the CASSCF(10,8) potential surface, shown in Figure 2, is also discontinuous. The solid line shows ΔE, the energy of a wave function of C_{2v} symmetry relative to that of a D_{2h}-symmetry wave function (i.e., $Q = 0$); this curve has a nonzero energy change, $\Delta E = -0.0064$ eV, at $Q = 0$, indicating a small discontinuity. However, as is clearly seen in the figure, the discontinuity in the derivative of the C_{2v}-symmetry surface at $Q = 0$ is pronounced. Note that, as expected, the energy decreases initially as pyrazine is displaced along ν_{12}.

Electronic-structure computational schemes which determine analytical harmonic vibration frequencies assume that the wave function is stable to symmetry lowering. When the wave function is unstable, they unwittingly report vibration frequencies, but the numbers reported are not necessarily meaningful. For the b_{1u} modes of $T_1(^3B_{3u})$ as calculated by UMP2 and CASSCF(10,8), all calculated frequencies (see the Supporting Information) appear reasonable except those for the mode most associated with lone-pair localization, ν_{12}, for which the calculated frequencies are 2380 and 2732 cm^{-1}, respectively. Further investigation reveals that single-determinant wave functions (and hence UMP2 results) are also unstable with respect to b_{1g} and b_{2g} displacements. While the calculated b_{1g} frequency for ν_{10a} of 22 042 cm^{-1} is clearly erroneous, the calculated b_{2g} frequencies for ν_4 and ν_5 of 1260 and 803 cm^{-1}, respectively, are quite plausible. Interestingly, these modes are perceived as being switched in order compared to those of the ground state. Whether or not such a switching actually occurs has been an issue of some controversy,[17] and the naive application of results such as this to resolve that controversy would have led to the incorrect conclusion. Hence, for analytical frequency calculations on excited states, it is imperative that the wave function be tested for stability before computed frequencies are interpreted. The CASSCF(10,8) wave function is stable with respect to b_{1g} distortions but remains unstable to b_{2g} ones.

A method which can be employed to establish the stability of CASSCF wave functions is state averaging. In this approach the CASSCF wave function is optimized to minimize the average energy of a number of electronic states. In calculations on $S_1(^3B_{3u})$ it has been usual practice[10,11,23] to obtain wave functions which mimimize the equally weighted average energy of $S_0(^1A_g)$, $S_1(^1B_{3u})$, and the close lying state $S_2(^1B_{2u})$. The result is a wave function which is completely stable to symmetry lowering, and in particular one that is very well suited to study the S_1-S_2 conical intersection. However, for our purposes it embodies excessive averaging and is not the most appropriate scheme. For the case of lone-pair localization distortions, symmetry lowering reveals two localized (diabatic) states, states corresponding to localization on each of the two nitrogens. These interact to form two (n,π*) adiabatic states, the lower being

TABLE 4: Comparison of Observed and Calculated $T_1(^3B_{3u})$ Vibration Frequencies, cm^{-1} [a]

el str method	vibr method	a_g, 8a	a_g, 9a	a_g, 1	a_g, 6a	b_{1u}, 12	a_u, 16a	b_{1g}, 10a	b_{2g}, 5	b_{2g}, 4	b_{3u}, 16b
observed[b]		1234[d]	1149	986	620	690[c]	406	254		295	236
B3LYP	AN	1571	1191	1029	617	667	448	84i	834	371	266
B3LYP	NUM	1577	1180	1035	613	1386	439	276	775	362	233
B3LYP-TDDFT	NUM	1587	1183	1037	613	1360	444	132	770	310	233
B3LYP	ANH	1562	1187	1026	614	1393	442	374	802	393	254
B3LYP-TDDFT	ANH	1576	1188	1025	613	1372	445	418	797	333	250
SVWN	AN	1574	1151	1039	598	831	432	378	795	487	241
SVWN	NUM	1545	1121	1026	591	1456	429	201	686	481	214
SVWN-TDDFT	NUM	1550	1120	1029	590	1397	440	65	678	481	204
SVWN	ANH	1523	1127	1038	592	1458	432	368	721	488	239
SVWN-TDDFT	ANH	1528	1124	1036	591	1404	441	395	711	477	227
CIS	AN	1724	1284	1097	658	406i	493	945i	911	992	322
CASSCF	AN	1663	1266	1053	643	2723*	457	370	834*	2343i*	311
CASSCF	NUM	1664	1266	1053	644	1347	461	280	853	1229	321
CASSCF	ANH	1664	1270	1052	645	1373	463	503	878	1091	332
UMP2	AN	1568	1197	1027	609	2380*	440	22042*	803*	1260*	269
CASPT2	NUM	1617	1196	1051	604	1594	389	203	720	2069	197
CASPT2	ANH	1587	1201	1022	604	1546	393	392	755	1824	225

[a] AN (analytical) frequencies are from analytical second-derivative calculations, while NUM (numerical) and ANH (anharmonic) frequencies are from analysis of the potential surfaces along the appropriate CASSCF analytical normal modes. An asterisk indicates that the potential-energy surface is not a continuous function of that particular mode; i indicates an imaginary frequency, i.e., a transition state. [b] From Fischer,[17] except for those described in footnote *c*. [c] Our assignment of an observed[30] infrared line; see the Conclusions. [d] We reassign this as 1410 cm^{-1}.

TABLE 5: Analytically Calculated and Observed non-CH Infrared-Active Vibration Frequencies, cm^{-1} [a]

method	state	b_{1u}, ν_{19a}	b_{1u}, ν_{18a}	b_{1u}, ν_{12}	b_{2u}, ν_{19b}	b_{2u}, ν_{14}	b_{2u}, ν_{18b}	b_{3u}, ν_{11}	b_{3u}, ν_{16b}
obsd 1	S_0	1484	1136	1021	1416	1149	1063	785	420
B3LYP	S_0	1508	1162	1032	1436	1089	1242	803	431
SVWN	S_0	1468	1142	1002	1405	1065	1333	767	410
SCF	S_0	1652	1251	1117	1553	1191	1117	888	484
CASSCF	S_0	1623	1225	1114	1527	1152	1080	829	455
MP2	S_0	1505	1160	1034	1448	1086	1360	804	420
obsd	T_1			690[b]				565[c]	236[17]
B3LYP	T_1	1381	1001	667	1349	1081	1331	733	266
SVWN	T_1	1350	1022	831	1329	1052	1417	701	241
CIS	T_1	1498	1100	406i	1464	1153	1189	809	311
CASSCF	T_1	1486	1063	[2723]	1447	1139	1362	741	311
UMP2	T_1	1421	1107	[2380]	1347	1078	1519	736	269

[a] Square brackets flag clearly erroneous frequencies associated with the potential surface being a discontinuous function of the b_{1u} coordinates. [b] Our assignment. [c] Tentative assignment.[29]

$T_1(^3B_{3u})$ and the upper $T_5(^3B_{2g})$. Hence, the most appropriate scheme to establish continuity with respect to b_{1u} distortions is an equal-weight state average of these two states. The resulting potential energy surface for distortion along ν_{12} is shown in Figure 2 and is continuous. Similarly, distortions along the b_{2g} modes ν_4 and ν_5 involve interactions between $T_1(^3B_{3u})$ and the (π,π^*) state $T_2(^3B_{1u})$, and we find that averaging over these states does indeed result in a continuous potential-energy surface.

While state averaging can eliminate discontinuities, it modifies the wave function from that which would otherwise be thought of as optimal and hence may modify key qualitative features. Figure 2 depicts a possible example of this as the single-state curves appear to have a double-minimum form, while the state-averaged surface shows only a single minimum. To determine which is the most appropriate qualitative description of the potential surface, CASPT2 calculations have been performed. In each case, the CASPT2 surface has a minimum at $Q = 0$, though the single-state surface is of course not continuous at this point. Further, the symmetry-broken CASPT2 energy is significantly *higher* than the D_{2h}-symmetry energy. These results indicate that it is indeed the state-averaged wave function which provides the best CASPT2 description of the potential surface. Finally, we optimized the geometry in C_{2v} symmetry with and without state averaging. With it, the geometry relaxed to a fully symmetric D_{2h} structure, but without

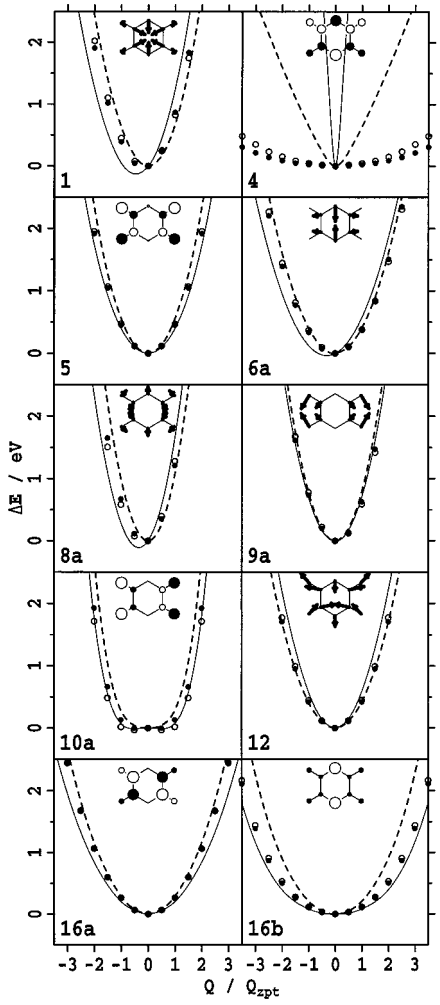

Figure 1. Change in pyrazine $T_1(^3B_{3u})$ potential energy on displacement of pyrazine along various CASSCF $T_1(^3B_{3u})$ normal modes, the displacements expressed in terms of the appropriate CASSCF zero-point vibration length Q_{zpt}. The energies are (—) CASPT2, (– –) CASSCF, (●) B3LYP, and (○) B3LYP-TDDFT. The insets show the form of the CASSCF normal modes.

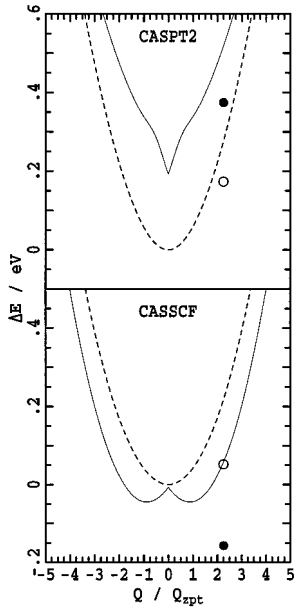

Figure 2. CASSCF and CASPT2 potential-energy surfaces of pyrazine $T_1(^3B_{3u})$ displaced along the b_{1u} CASSCF normal mode ν_{12}. The energies are (—) the reference CASSCF wave function optimized for $T_1(^3B_{3u})$ only, (– –) the reference CASSCF wave function optimized for an equal-weight state average of $T_1(^3B_{3u})$ and $T_5(^3B_{1u})$, (●) the single-state energy of the structure obtained by minimizing the single-state CASSCF energy in C_{2v} symmetry, and (○) the state-averaged energy at this geometry. The energy ΔE is expressed relative to that obtained at $Q = 0$ using D_{2h} electronic symmetry so that continuous potential-energy surfaces must pass through the point ($Q = 0$, $\Delta E = 0$); however, electronic symmetry lowering discontinuously reduces the single-state CASSCF energy at $Q = 0$ while raising the corresponding CASPT2 energy.

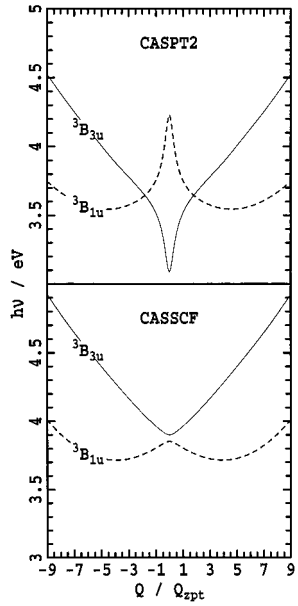

Figure 3. CASSCF and CASPT2 potential-energy surfaces of pyrazine $T_1(^3B_{3u})$ and $T_2(^3B_{1u})$ displaced along the b_{2g} CASSCF normal mode ν_4, the CASSCF reference wave function being obtained from an equal-weight state average over these two states.

it a localized minimum-energy structure is found. The coordinate change was projected onto the CASSCF normal modes and found to be $2.2Q_{zpt}$, and this point is indicated in Figure 2. CASPT2 calculations at this geometry result in an energy which is again well above the D_{2h} CASSCF energy. Hence, at the CASPT2 level, there is no tendency to form localized structures.

In CASSCF potential energy surfaces, discontinuities can arise at configurations of other than high symmetry due to the swapping of orbitals to and from the selected active space. Effects such as this can be minimized by careful choice of the initial orbitals in the CASSCF calculations, and through level shifting. Also, discontinuities at the high-symmetry geometry can occur if, in low symmetry, the orbitals selected for the active space do not precisely correspond to those used in the high-symmetry calculation. Both of these effects can be eliminated by expanding the active space to include all relevant orbitals. Initially, we strove to find an active space which could produce a potential surface continuous for several zero-point displacements in any combination of modes around the $^3B_{3u}$ equilibrium geometry. However, it soon became clear that such an active space would need to be at least as large as (12,14), the active space which contains all molecular orbitals within the range of the lowest occupied π orbital to the highest unoccupied π^* valence orbital. In practice, additional orbitals are needed as the inclusion of an orbital with significant nitrogen lone-pair involvement requires the addition of the matching orbital with opposite phase, for example, and hence, all orbitals of intermediate energy between these and those in the (12,14) active space must also be included. As a result, no practicable single active space can be found, and hence active spaces and state-averaging specifications were designed for each individual mode, as detailed in Table 1. The resulting potential energy surfaces, shown in Figure 1, are continuous. Both removal and addition of orbitals from these active spaces will, in general, result in loss of continuity. The choice of active space is particularly critical for ν_4 and ν_5.

CIS wave functions are not subject to instabilities, provided that the ground-state wave function is stable, as they embody a complete configuration-interaction calculation at the single-excitation level; i.e., all molecular orbitals are treated equally. However, density functional calculations can also give rise to instabilities in the solutions of the Kohn−Sham equations.[28] For pyrazine, we find that the B3LYP and SVWN $^3B_{3u}$ potential surfaces are continuous.

In the Duschinsky-matrix summary given in Table 3, vibrational symmetries for which distortion is known to give rise to discontinuous potential energy surfaces are flagged by "D"; other cases in which discontinuity is suspected are flagged with "d".

C. Vibronic Coupling. What is usually termed "vibronic coupling" involves the breakdown of the crude-adiabatic approximation, i.e., the assumption that the combined electronic/vibrational wave functions can be expressed as

$$\psi_{ij}(\mathbf{q},\mathbf{Q}) = \phi_i(\mathbf{q};\mathbf{Q}_0)\,\chi_j(\mathbf{Q}) \qquad (1)$$

where i indexes electronic states and j indexes vibrational states, $\mathbf{q}$ are electronic coordinates, $\mathbf{Q}$ are nuclear coordinates, and the electronic wave functions ϕ_i, which depend parametrically on $\mathbf{Q}$, are taken to be invariant to $\mathbf{Q}$ and hence are evaluated at some reference configuration $\mathbf{Q_0}$ only. In this fashion the excited-state vibrational modes and frequencies are often simply taken to equal those of the ground electronic state. Vibronic coupling in its simpler Herzberg−Teller form[15] involves merely the reintroduction of coordinate dependence to the electronic wave functions ϕ_i. More generally, the full molecular Hamiltonian $\mathbf{H_D}$, which includes nonadiabatic interactions, can be expressed in the basis set of the crude-adiabatic wave functions; applying a first-order Taylor expansion in nuclear motion gives interstate ($i \neq i'$) matrix elements

$$\langle\psi_{ij}|\mathbf{H_D}|\psi_{i'j'}\rangle = \sum_k \left\langle \phi_i \left| \frac{\partial \mathbf{H_D}}{\partial Q_k} \right| \phi_{i'} \right\rangle \langle\chi_j|Q_k|\chi_{j'}\rangle = \sum_k \alpha_k^{ii'} \langle\chi_j|Q_k|\chi_{j'}\rangle \tag{2}$$

where k indexes the normal modes and the α's are known as vibronic coupling constants. (Note that vibronic coupling constants are often[15,17] expressed as $2^{1/2}\alpha_k^{ii'}$.) If only two electronic states are involved, these are expressed simply as α_k. The nuclear wave functions $|\chi_j\rangle$ are usually expressed as products of harmonic oscillator wave functions containing n^j_k quanta in each mode so that the above vibrational integrals are zero except for the case that $n^j_l = n^{j'}_l$ for $l \neq k$ and $n^j_k = n^{j'}_k \pm 1$; in this case we obtain[46]

$$\langle\chi_j|Q_k|\chi_{j'}\rangle = [\max(n^j_k, n^{j'}_k)/2]^{1/2} \tag{3}$$

if Q_k is expressed in (mass-dependent) dimensionless zero-point units. The interactions involved are shown schematically in Figure 4 for the case of two electronic states and one vibrational degree of freedom. This is equivalent to assuming that there exist two delocalized diabatic states with coordinate-dependent coupling given by

$$\mathbf{H_D} = \begin{bmatrix} h_0 + \sum_k \frac{h\nu_k}{2}[Q_k^2 + \dot{Q}_k^2] & \sum_k \alpha_k Q_k \\ \sum_k \alpha_k Q_k & h_0 + \Delta + \sum_k \frac{h\nu_k}{2}[Q_k^2 + \dot{Q}_k^2] \end{bmatrix} \tag{4}$$

where $\dot{Q}_k$ is the momentum conjugate to Q_k, h_0 is the energy of the lower state, and Δ is the energy difference.

An alternate but equivalent description of this model can be obtained through a coordinate-independent rotation of this Hamiltonian into the localized diabatic representation[25]

$$\mathrm{HL} = \begin{bmatrix} h_0 + \frac{\Delta}{2} + \sum_k \frac{h\nu_k}{2}[(Q_k + \delta_k)^2 + \dot{Q}_k^2 - \delta_k^2] & J \\ J & h_0 + \frac{\Delta}{2} + \sum_k \frac{h\nu_k}{2}[(Q_k - \delta_k)^2 + \dot{Q}_k^2 - \delta_k^2] \end{bmatrix} \tag{5}$$

where

$$\Delta = 2|J| \quad \text{and} \quad \delta_k = \alpha_k/h\nu_k \tag{6}$$

In this representation, J is the electronic coupling between two equivalent symmetry-broken localized states, each state being characterized by displacements δ_k in the equilibrium geometry. These diabatic surfaces are sketched in Figure 5, which illustrates an important property, the vibrational mode relaxation energy λ_k given by

$$\lambda_k = 2h\nu_k\delta_k^2 = 2\alpha_k^2/h\nu_k \tag{7}$$

This representation is the one most frequently used to describe intramolecular electron-transfer processes, processes which involve very strong vibronic coupling between the ground and first excited electronic states. Computationally, one proceeds by defining vibrational/electronic wave functions for each of the localized states here named L and R:

$$\psi_{Lj}(\mathbf{q},\mathbf{Q}) = \phi(\mathbf{q};\boldsymbol{\delta})\,\chi_j(\mathbf{Q}+\boldsymbol{\delta}) \quad \text{and} \quad \psi_{Rj}(\mathbf{q},\mathbf{Q}) = \phi(\mathbf{q};-\boldsymbol{\delta})\,\chi_j(\mathbf{Q}-\boldsymbol{\delta}) \tag{8}$$

The vibronic coupling matrix elements from eq 5 are then given by

$$\langle\psi_{Lj}|\mathbf{H_L}|\psi R_{j'}\rangle = J\langle\chi_j(\mathbf{Q}+\boldsymbol{\delta})|\chi_{j'}(\mathbf{Q}-\boldsymbol{\delta})\rangle \tag{9}$$

which is simply the electronic coupling times a Franck−Condon overlap matrix element. Note that all of these equations can be generalized to the situation in which the localized diabatic surfaces are not degenerate,[25] but that case is not of concern here.

Another method by which this vibronic problem could be solved is through the introduction of the Born−Oppenheimer adiabatic approximation to diagonalize either eq 4 or eq 5 parametrically as a function of $\mathbf{Q}$ and hence determine two anharmonic adiabatic electronic potential surfaces here named "+" and "−". The resulting surfaces (for $\Delta = 4h\nu$ and $\lambda = 8h\nu$) are shown in Figure 5; they can subsequently be used in variational calculations and individual vibrational wave functions

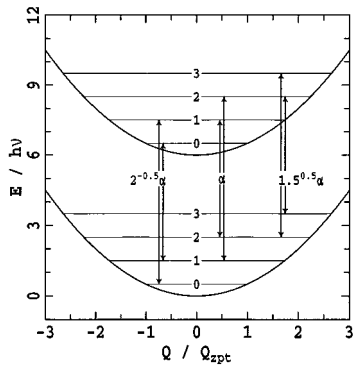

Figure 4. Physical interpretation of the delocalized diabatic vibronic coupling model. Shown are the two potential energy surfaces and their vibrational eigenstates coupled via eq 4 for $h_0 = 0$ and $\Delta = 6h\nu$, along with arrows indicating the nonzero inter-vibronic-level couplings specified by eqs 2 and 3.

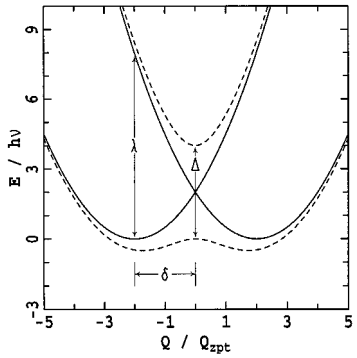

Figure 5. An alternate but equivalent description of the vibronic coupling problem in terms of equivalent localized diabatic states shown as solid lines for the situation in which $h_0 = 0$, $\Delta = 2|J| = 4h\nu$, and $\delta = 2Q_{zpt}$; derived parameters include the vibronic coupling constant $\alpha = 2h\nu$ (from eq 6) and reorganization energy $\lambda = 8h\nu$ (from eq 7). Also shown as dashed lines are the Born−Oppenheimer adiabatic surfaces obtained by diagonalizing either eq 4 or eq 5 parametrically as a function of Q. The situation depicted here is one of strong vibronic coupling as $\lambda > \Delta$, and the lower Born−Oppenheimer surface is therefore a double minimum; see eq 11.

determined for each state:

$$\psi_{-j}(\mathbf{q},\mathbf{Q}) = \phi_{-}(\mathbf{q};\mathbf{Q})\,\chi_j^{-}(\mathbf{Q}) \quad \text{and}$$
$$\psi_{+j}(\mathbf{q},\mathbf{Q}) = \phi_{+}(\mathbf{q};\mathbf{Q})\,\chi_j^{+}(\mathbf{Q}) \quad (10)$$

Not only are these adiabatic surfaces anharmonic, but the curvature at $\mathbf{Q} = 0$ is modified also so that the harmonic approximation for the vibration frequencies yields

$$\nu_k^{\pm} = \nu_k(1 \pm \lambda_k/\Delta)^{1/2} \quad (11)$$

The upper surface thus increases in curvature while that for the lower surface decreases. At $\Delta = \lambda_k$ the curvature of the lower state vanishes, and for larger coupling a double-minimum potential is produced, as depicted in Figure 5. Clearly the delocalized diabatic description is the most appropriate one for small vibronic coupling ($\lambda_k < \Delta$) while the localized diabatic description is most appropriate for large coupling. Figures 1−3 show calculated adiabatic potential energy surfaces for pyrazine, and surfaces for which the curvature is positive, near zero, and negative are readily apparent, indicating differing degrees of vibronic coupling strength (further, for all states of pyrazine considered, Table 3 indicates all symmetry blocks which contain double-minimum potentials).

In the localized diabatic approach, the dipole moment operator is given by

$$\mathbf{M_D} = \begin{bmatrix} 0 & -er/2 \\ -er/2 & 0 \end{bmatrix} \quad (12)$$

where e is the magnitude of the charge on the electron and r is the Cartesian distance through which an electron moves when transferred from one localized diabatic state to the other. It is given by

$$r = 2\delta Q_{\text{zpt}}/(\text{vibrational effective mass})^{1/2} \quad (13)$$

In eq 12, the diagonal elements simply represent the dipole moments of the two diabatic states. This operator in the delocalized diabatic representation transforms to

$$\mathbf{M_L} = \begin{bmatrix} 0 & -er/2 \\ -er/2 & 0 \end{bmatrix} \quad (14)$$

in which case $-er/2$ is simply interpreted as the transition moment linking the two delocalized diabatic states. Once either the delocalized or localized diabatic Hamiltonians (eq 2 or 9) are constructed and diagonalized, final vibronic-state dipole moments and inter-vibronic-state transition moments may be obtained from the appropriate electronic-dipole operator.

The electronic-dipole operators above may be transformed into the Born−Oppenheimer representation using

$$\mathbf{M} = \mathbf{C_L}^{\dagger}(\mathbf{Q})\mathbf{M_L}\mathbf{C_L}(\mathbf{Q}) = \mathbf{C_D}^{\dagger}(\mathbf{Q})\mathbf{M_D}\mathbf{C_D}(\mathbf{Q}) \quad (15)$$

where $\mathbf{C_L}$ and $\mathbf{C_D}$ parametrically diagonalize the electronic Hamiltonians $\mathbf{H_L}$ and $\mathbf{H_D}$, respectively. In this way the Born−Oppenheimer dipole and transition-moment operators become explicitly nuclear coordinate dependent, allotting intensity to what would otherwise be "forbidden" transitions.

For the evaluation of both energies and transition moments, the localized or delocalized diabatic formalisms, in the limit of infinite vibrational basis sets, yield identical results; use of the adiabatic approach, however, does not. First, we note that it does yield the correct answers in both the limit of very small vibronic coupling, $\lambda_k \ll \Delta$, and the limit of very large vibronic coupling, $\lambda_k \gg \Delta$. In the first limit, eq 11 reduces to

$$\nu_k^{\pm} = \nu_k \pm \alpha_k^2/\Delta \quad (16)$$

This result is readily obtained by determining the change in the level spacing shown in Figure 4 through application of first-order perturbation theory using the matrix elements given by eq 3. In the strong-coupling limit, the two localized potential wells become very deep and the harmonic vibration frequencies at the bottom approach ν_k. It is in the region of intermediate coupling with $\lambda_k \approx \Delta$ that the adiabatic approximation performs poorly; numerical examples of this are given elsewhere.[25] Equations 4 and 5 embody explicit coupling between the nuclear and electronic coordinates which alone results in nonzero values for the matrix elements associated with Born−Oppenheimer breakdown[15]

$$\left\langle \phi_{\pm}(\mathbf{q},\mathbf{Q}) \middle| \frac{\partial}{\partial \mathbf{Q}} \middle| \phi_{\pm}(\mathbf{q},\mathbf{Q}) \right\rangle \quad \text{and} \quad \left\langle \phi_{\pm}(\mathbf{q},\mathbf{Q}) \middle| \frac{\partial^2}{\partial \mathbf{Q}^2} \middle| \phi_{\pm}(\mathbf{q},\mathbf{Q}) \right\rangle \quad (17)$$

Once these nonadiabatic effects are included, the adiabatic formalism yields the same results as do the diabatic formalisms.

To date the most significant attempts to interpret the excited-state vibrations of pyrazine are the vibronic coupling calculations of Fischer[17] and the (hereto less-relevant) studies of the S_1-S_2 conical intersection by Domcke et al.[10,11] Fischer performed vibronic coupling calculations for the $S_1(^1B_{3u})$ and $T_1(^3B_{3u})$ states interacting with other states via ν_4, ν_5, and ν_{10a} using the delocalized diabatic approach; see Figure 4 and eq 4. For $T_1(^3B_{3u})$, he also allowed for spin−orbit interactions, primarily to calculate transition moments for the $S_0 \rightarrow T_1$ transitions. These were empirical calculations, and unperturbed frequencies ν, vibronic coupling constants α, and state energy gaps Δ were determined by fitting the available experimental data. Confidence in the results stems from the ability of the calculations to reproduce isotopic effects and singlet−triplet differences, but the fitted triplet energy gaps differ significantly from those evaluated by ab initio techniques[47] and suggest an alternative assignment of the observed electronic states; our recent ab initio and density-functional calculations[27] and other recent CCSD(T) calculations[14] suggest that the original ab initio results are reliable, but cannot discount the possibility that the energy gaps are indeed as Fischer's calculations suggest.[17]

A key assumption that is used in Fischer's calculations[17] is that only the nearest state of appropriate symmetry is involved in vibronic coupling with $S_1(^1B_{3u})$ and $T_1(^3B_{3u})$. There would appear to be little doubt that the selected states are the most important states, but nevertheless states of higher energy can also contribute. In fact, as the (n,π^*) transition involves considerable lowering of intraring bond orders, any excited state involving similar bond-order lowering would be expected to contribute. Fischer implicitly accounts for this effect in his calculations by optimizing the preinteraction vibration frequencies ν, decreasing them significantly compared to the ground-state values. However, he assumes that this process involves no Duschinsky rotation, and that the vibrational modes do not interchange in order. No estimates have been made of the uncertainties of the energy-gap parameters deduced from the model, and it is, in principle, possible that the differences in the energy gaps found between Fischer's results and those of electronic-structure calculations could be attributed to neglect of vibronic coupling with higher states.

The calculations which we perform here are all within the adiabatic Born−Oppenheimer approximation. These have the

advantage that they include all interactions with high-lying states, and in the analytical frequency calculations the Duschinsky matrixes are calculated rather than assumed. However, they neglect the effects of the nonadiabatic coupling terms shown in eq 17, which, for the most-important lowest-lying state, are included in Fischer's approach.[17] These contributions are large when $\lambda_k/\Delta \approx 1$ corresponding to intermediate strength vibronic coupling and are small otherwise. As deduced by Fischer,[17] this ratio is, in his notation, $V_k^2/(h\nu\Delta E_{t't})$, which evaluates to 0.31, 0.19, and 0.05 for ν_{10a}, ν_4, and ν_5, respectively. Hence, nonadiabatic effects are expected to be most significant for ν_{10a}.

D. Analysis of the Potential-Energy Curves for $T_1(^3B_{3u})$. Interpretation of the potential-energy curves shown in Figure 1, obtained as B3LYP, B3LYP-TDDFT, CASSCF, and CASPT2 energies evaluated along CASSCF normal coordinates, as well as the vibration frequencies shown in Table 4 deduced from these curves, raise six issues.

(i) Interpretation of the Unphysical Analytical Frequencies Appearing in Table 4. This issue has already been addressed in detail in section IV.B: they arise from instabilities in the wave function that also manifest themselves as discontinuous potential-energy surfaces. In the potential-energy surface calculations, these problems are overcome through the use of expanded active spaces and state averaging, as detailed in Table 1.

(ii) Comparison of Calculated and Experimental Frequencies. As mentioned in the overview, good agreement is obtained for five of the eight observed frequencies, with discrepancies appearing for ν_4, ν_{8a}, and ν_{10a}. If ν_{12} had been observed, large discrepancies would also be found for this mode as well, but the theoretical predictions for ν_5 are reasonably self-consistent.

(iii) Comparison of Surfaces and Frequencies Evaluated by Different Electronic-Structure Methods. Quantitative differences in the potential-energy surfaces appear for the totally symmetric modes ν_1, ν_{6a}, and ν_{8a} as changes in equilibrium geometry rather than as changes in frequency. The CASSCF curvature is distinctly larger than that predicted by the other methods for ν_{16b}, but all surfaces are qualitatively similar. For all other modes, very similar results are predicted by the different methods, with the exception of ν_4 for which large differences appear. The B3LYP and B3LYP-TDDFT results indicate a much lower curvature ($\nu_4 = 371$ and 333 cm^{-1}, respectively) than the CASSCF results ($\nu_4 = 1229$ cm^{-1}), while a much higher curvature is predicted by CASPT2 ($\nu_4 = 2069$ cm^{-1}). From Figure 3 the origin of the problems with CASSCF and CASPT2 can be seen. CASSCF incorrectly locates $T_2(^3B_{1u})$ below $T_1(^3B_{3u})$, and these states are mixed by ν_4 (b_{2g}). Very strong vibronic coupling resulting in a double-well potential for $^3B_{1u}$ is thus predicted by CASSCF, with the concurrent elevation of the frequency of the upper state. Dynamic electron correlation favors $^3B_{3u}$ over $^3B_{1u}$ and correctly reorders these states. However, the conical intersection predicted at the CASSCF level has profound effects on the CASPT2 results, with the dynamic electron correlation energy decreasing rapidly as the geometry is distorted. Hence, while CASPT2 adequately corrects CASSCF energies, it is not able to correct the shape of the potential-energy surface. A new computational method known as "multistate" CASPT2 has recently been developed by Finley, Malmqvist, Roos, and Andrés[48] to obtain improved potential-energy surfaces for problems of this type.

(iv) Comparison of Harmonic Frequencies Obtained Analytically and Numerically. The numerical harmonic frequencies in general are not exactly equal to the analytical ones as the displacement is made along the CASSCF normal mode direction, not the native normal mode direction. The differences are small, on the order of 10 cm^{-1}, indicating that the form of normal modes is usually robust. Another difference arises when the analytical frequency is imaginary as the numerical frequency is obtained from a harmonic expansion about the potential minimum and remains real. In this case the numerical frequency is the one most relevant to experiment, especially (as in the case of ν_{10a} by B3LYP) if the double-minimum potential is very shallow. Analytical normal modes are only available for a selected set of electronic-structure methods (herein CASSCF, CIS, SVWN, and B3LYP) and are not currently available for desirable methods such as CASPT2 and TDDFT approaches. When the normal mode direction is insensitive to the computational method, it is possible to determine vibration frequencies using advanced electronic-structure methods using the normal mode directions determined by simpler schemes such as CASSCF. However, for pyrazine there is one exception, ν_{12}. As the CASSCF wave function is unstable with respect to distortion along ν_{12}, the analytical CASSCF frequency is poorly determined. It happens that the calculated frequency is 2723 cm^{-1} so that ν_{12} interacts erroneously with the CH stretch, ν_{13}. Hence, displacement along the CASSCF ν_{12} direction provides in this case a very poor coordinate for the numerical evaluation of vibration frequencies by other methods.

(v) Importance of Diagonal Anharmonicity. For most modes, anharmonicity has only a small affect, but its importance grows as the vibronic coupling strength increases, becoming on the order of 10 cm^{-1} for ν_{12}, 30 cm^{-1} for ν_4 and ν_5, and 100−300 cm^{-1} for ν_{10a}. This pattern is qualitatively consistent with Fischer's vibronic coupling analysis,[17] which was not required for ν_{12}, reflected small coupling for ν_4 and ν_5, and indicated large coupling for ν_{10a}. In fact the anharmonicity of ν_{10a} is readily apparent from Figure 1, with all methods indicating near-zero or slightly negative curvature at $Q = 0$. Quantitatively, zero curvature is expected for $\lambda_k/\Delta = 1$, a value considerably higher than that deduced by Fischer, 0.31. However, most calculated harmonic vibration frequencies indicate that ν_{10a} is depressed in frequency from the ground-state value by ca. the experimental value, 665 cm^{-1}, the exception being CIS which predicts a depression of 1900 cm^{-1}. Anharmonic corrections increase the predicted frequency to typically 200 cm^{-1} above the observed frequency, however. This increase could be an artifact as only diagonal anharmonicity is included in calculations, and as the CASSCF frequency is low so that Q_{zpt} is large, the Cartesian displacements in ν_{10a} involve large-amplitude motions which are better represented using curvilinear coordinates than (rectilinear) normal modes. Hence, off-diagonal anharmonicity for this mode is expected to be large and act to reduce the calculated vibration frequency. Nonadiabatic effects arising from the vibronic coupling (eq 17) are also not included in our calculation; these will depress the vibration frequency and are largest when $\lambda_k/\Delta = 1$.

(vi) Differences between Direct and Time-Dependent DFT Methodologies. While it is possible to perform direct density-functional calculations for triplet excited states, no analogous approach exists for singlet states due to spin contamination problems.[27] Time-dependent (TDDFT) approaches can be equally applied in both cases, however, and so here we have the opportunity to consider the performance of these more approximate methods compared to direct evaluation. In general, agreement between the two approaches is very good, to within a few inverse centimeters. However, as the effects of vibronic coupling increase, differences of up to 150 cm^{-1} appear.

V. Conclusions

In general, we find that most computation methods perform very well for ground-state vibrations, especially after scaling, but variable results are obtained for the vibrations of $T_1(^3B_{3u})$. Of the eight modes for which frequencies have been firmly assigned,[17] good results are obtained for five: ν_1, ν_{6a}, ν_{9a}, ν_{16a}, and ν_{16b}. This includes the prediction of the rather unusual frequency increase observed[17,49] for ν_{16a} (observed 65 cm^{-1}, calculations range between 51 and 130 cm^{-1}), a result usually interpreted in terms of vibronic coupling between $S_0(^1A_g)$ and $S_3(^1A_u)$. Also, the observed 40% reduction in ν_{16b} is well reproduced, this mode posing[49] an anomaly for theories which assume that important vibronic coupling only arises with nearby electronic states, which, in this case, are nonexistent. Indeed, it is likely that most excited-state modes are well represented by these theoretical approaches, just like ground-state modes. However, this is not always the case for modes which are involved in strong vibronic coupling. Interestingly, it is these vibronically active modes which are readily detectable in absorption and emission spectra, and hence they are the ones for which the greatest interest often lies.

In particular, the application of CASSCF-based methods to study excited-state vibrations of molecules of the size of pyrazine appears fraught with difficulties. For analytical CASSCF frequency calculations, unstable wave functions are likely and will lead to possibly undetected erroneous frequencies. To avoid this problem, active spaces must be carefully chosen and extensive state averaging may be necessary.[50] Not all vibrational modes are beset with these problems, of course, and many degrees of freedom can be faithfully modeled using CASSCF; the limitation is, however, that it is modes associated with vibronic activity that lead to unstable wave functions and discontinuous potential-energy surfaces, but it is these modes for which the greatest interest usually lies. Other difficulties arise as dynamic electron correlation, accounted for in CASPT2 but not in CASSCF calculations, often controls the relative energies of excited states. If CASSCF incorrectly places the excited state of interest above or very close to another excited state, its potential-energy surface will be dominated by conical intersection effects. While CASPT2 may correct the relative energies of the states, it is not capable of correcting the shape of the potential energy surface in such instances. Hence, anomalous results are obtained, and the use of the new multistate CASPT2 method[48] appears essential.

CIS appears preferable to CASSCF for the determination of analytical frequencies as discontinuities and unstable wave functions rarely arise; this method is typically much more efficient as well. However, we obtained quality results only for the modes that do not involve vibronic coupling. Erratic results were obtained for modes that do involve vibronic coupling, with the frequency lowering being dramatically overestimated for ν_{10a} and ν_{12} but almost nonexistent for ν_4.

It is clear from these calculations that, even possibly for singlet states, density-functional normal coordinates would be much easier to use than CASSCF and possibly also CIS normal coordinates in the construction of potential-energy curves using methods such as CASPT2.

Indeed, the best results were obtained using density-functional theory, with both the simplistic SVWN functional and the sophisticated B3LYP functional producing quantitatively accurate results for vibronically inactive modes and realistic descriptions of modes involving vibronic coupling. For example, in $T_1(^3B_{3u})$ the observed frequency of ν_{10a} is reduced by a factor of 4 from its ground-state value due to vibronic coupling, and the calculations predict factors of 3−5. Hence, the most vibronically active mode is correctly identified. A large depression of ν_4 and a small depression of ν_5 are also predicted, in good agreement with experiment. This is a significant achievement as originally[16] it was thought that ν_5 was depressed the most and moved to a lower frequency than ν_4, later experiments[17] showing that this is not the case. The only credible estimates of ν_{12} are those obtained from the analytical density-functional approaches which predict 667 cm^{-1} (B3LYP) and 831 cm^{-1} (SVWN). These results do indicate significant vibronic activity, the ground-state value being 1021 cm^{-1}. This mode has not been experimentally assigned for $T_1(^3B_{3u})$ although it is observed[6,50,51] at 636 cm^{-1} for $S_1(^1B_{3u})$. The B3LYP analytical frequency for the spin-contaminated[27] "average" S_1-T_1 pair is 646 cm^{-1}, and so a crude estimate of the actual frequency in T_1 would be $636 + 2 \times (667 - 646) = 678$ cm^{-1}; an infrared active mode has been observed[30] in T_1 at 690 cm^{-1}, and we have assigned this frequency to ν_{12} in Table 4. Density-functional methods may thus prove very useful in the interpretation of excited-state molecular spectra, and new functionals are being developed for this purpose.[52]

Analytical frequency calculations for excited states often predict some small imaginary vibration frequencies. From these calculations, an example is ν_{10a} for which the B3LYP frequency is 84i cm^{-1}. In such cases, it is essential that the potential surface be determined for finite displacements along the normal mode as the resulting surface most likely contains a very shallow local minimum. In this case, harmonic analysis of the resulting surface about its minimum predicts a vibration frequency of 276 cm^{-1}, and it is clear that the double-minimum potential cannot sustain localized zero-point vibration. While anharmonic corrections increase the frequency further to 374 cm^{-1}, the observed value is 254 cm^{-1}. Hence, the result which is obtained directly from the analytical frequency calculation provides a rather poor description of the molecular vibration.

Often it is possible to "diabatize" Born−Oppenheimer potential-energy surfaces. This involves taking the computed surfaces and constructing a diabatic electronic Hamiltonian of the form of either eq 4 or eq 5 from these. While all calculation methods indicate that significant vibronic coupling is involved with ν_{12} of $T_1(^3B_{3u})$, attempts at diabatizing the calculated surfaces for $T_1(^3B_{3u})$ and $T_5(^3B_{2g})$ have proven unsuccessful. This indicates that the dominant state involved with $T_1(^3B_{3u})$ lies higher in energy than $T_5(^3B_{2g})$. While ν_{12} has been identified[6,51,52] in the spectrum of $S_1(^1B_{3u})$, it is yet to be identified in the spectrum of $T_1(^3B_{3u})$. For weak vibronic coupling, perturbation theory predicts that the frequency depression is given by α_k^2/Δ (eq 16), whereas the absorption intensity is proportional to α_k^2/Δ^2. Hence, vibronic coupling to higher excited states will be proportionally more effective in reducing the vibration frequency than in providing intensity, and this could explain the lack of observation of this mode in the spectrum of the triplet state.

All calculations for ν_{8a} suggest that its frequency should be 300−400 cm^{-1} higher than that of the absorption line assigned[17] to it at 1234 cm^{-1}. To investigate this further, we evaluated the frequency for ν_{8a} in $S_1(^1B_{3u})$ analytically using CASSCF, CIS, and (spin-contaminated[27]) B3LYP. Again, the calculated values (see the Supporting Information) exceed the observed[17] value of 1373 cm^{-1} by 200−300 cm^{-1}, indicating that there may be some specific problem with this mode. However, all methods predict that the triplet-state frequency should exceed that of the singlet state by 20−40 cm^{-1}, whereas the observed assignment places the triplet frequency lower by 139 cm^{-1}. Further, all

calculations predict that perdeuteration should reduce the frequency by 30−50 cm^{-1}, whereas the experimental assignments indicate an increase of 31 cm^{-1}. It is hence quite likely that the very weak line observed[16] at 1234 cm^{-1} in the $S_0 \rightarrow T_1$ spectrum is not due to ν_{8a}. In the phosphorescence excitation spectrum[29] of pyrazine a line at 1410 cm^{-1} is observed and attributed to $8a^1_0\ 6a^1_0\ 10a^2_0$. This is questionable as $10a^2_0$ itself is poorly identified and no other sequence band involving both $6a^1_0$ and $10a^2_0$ is reported. On the basis of our calculations, it appears reasonable that the band at 1410 cm^{-1} be assigned to ν_{8a}.

It is a general observation[15,17] that vibronic coupling between two electronic states usually has the effect of depressing all frequencies of a particular symmetry of the lower state such that the relative ordering of the modes remains invariant. This picture no longer remains generally true if significant vibronic coupling to a number of excited states occurs, however. Often, in assigning the spectra of excited states, it is necessary to assume some particular ordering of the excited-state frequencies. This is tantamount to assuming properties of the appropriate Duschinsky rotation matrix. A priori Born−Oppenheimer analytical frequency calculations have the advantages that they make no assumptions as to the number of states involved in the vibronic coupling, and the Duschinsky matrixes are deduced from the calculations. The Duschinsky-matrix summary table, Table 3, indicates for which irreducible representations in any of the excited states considered the relative order of normal modes swap ("S") or the normal modes strongly mix ("M"). We see that, for the out-of-plane modes, which are often the most vibronically active modes, very few deviations from simple behavior are reported, in line with the general observations discussed earlier. However, the in-plane b_{2u} and b_{3g} modes are involved in a large number of mode swaps. These swaps are associated with specific bond weakening that arise due to the electronic transition.

Recently, Kok et al.[30] observed the infrared absorption spectrum of pyrazine T_1 as the transient change in the phosphorescence spectrum (in dodecane matrix at 1.3 K) induced by infrared laser excitation. The spectrum appears among that of the S_0 ground state and that of the matrix and hence requires careful analysis. A total of seven bands within the region of 250−1600 cm^{-1} were attributed to infrared-active vibrations of pyrazine T_1, these being located at 565, 584, 623, 690, 820, 939, and 1103 cm^{-1}. To interpret these data, all calculated infrared-active non-CH vibration frequencies are shown in Table 5 for both S_0 and T_1, along with known or potential assignments. Earlier, we assigned the line at 690 cm^{-1} to ν_{12}, and this assignment is discussed no further.

Tomer et al.[29] have tentatively assigned an observed line in the phosphorescence excitation spectrum observed at 800 cm^{-1} as the overtone band $11^1_0\ 16b^1_0$, suggesting 563 cm^{-1} for ν_{11}. This frequency coincides with a very weak peak found by Kok et al.[30] at 565 cm^{-1}. Like ν_{16b}, ν_{11} is of b_{3u} symmetry. All computational methods produce continuous potential-energy surfaces in the two b_{3u} modes, and the results for ν_{16b} are quite good, with errors ranging from 5 to 95 cm^{-1}. However, the computed analytical vibration frequencies for ν_{11} exceed 565 cm^{-1} by 136−234 cm^{-1}, while, for S_0, these methods produce errors in the calculated frequency of just −18 to +46 cm^{-1}. The strongest argument supporting the assignment of $\nu_{11} = 565$ cm^{-1} comes from the analogy with S_1 for which ν_{11} is firmly assigned[53] as 577 cm^{-1}, with our CASSCF and CIS calculations both predicting small changes for ν_{11} between S_1 and T_1. However, these assignments imply that ν_{11} is depressed further than ν_{16b} as a result of vibronic coupling, and hence one would expect to see 11^1_0 in both the $S_0 \rightarrow S_1$ and $S_0 \rightarrow T_1$ spectra, but the required lines have not been observed. Nevertheless, anomalies of this type are well-known[53] for S_1. Another apparent inconsistency in the experimental data is that the peak in their spectrum which Kok et al. assign to ν_{11} in S_0 is one of the most intense peaks in the spectrum, while that for T_1 is extremely weak.

Unfortunately, it is not possible to suggest assignments for the bands observed[30] at 584, 623, 820, 939, and 1103 cm^{-1}. The calculated frequencies with which we would hope to correlate these bands, obtained as the observed S_0 frequency plus the calculated frequency change in going from S_0 to T_1, are 1330−1400 cm^{-1} for ν_{19a}, 1320−1350 cm^{-1} for ν_{19b}, 1130−1240 cm^{-1} for ν_{18b}, 1140 cm^{-1} for ν_{14}, and 1080−1100 cm^{-1} for ν_{18a}. Of particular note is ν_{18} for which all methods predict a significant frequency *increase* in T_1 compared to the (observed) S_0 value of 1063 cm^{-1}. In the experimental spectra many of the lines attributed to T_1 fundamentals were very weak, while strong lines observed at 811, 1029, and 1076 cm^{-1} were assigned[30] to crystal site effects. It could be that some of these strong lines actually correspond to pyrazine fundamentals instead. Also, the dodecane crystal matrix absorbs strongly in the 1200−1400 cm^{-1} region, and it is possible that pyrazine fundamentals located in this congested region were obscured.

Acknowledgment. P.W. is indebted to the Swiss National Science Foundation for support, while J.R.R. is indebted to the Australian Research Council. We thank Dr. George Bacskay from the University of Sydney for helpful discussions.

Supporting Information Available: In ASCII format are provided 30 sets of optimized coordinates, energies, vibration frequencies, normal modes, displacements, and reorganization energies expressed in terms of normal mode contributions, and complete Duschinsky rotation matrixes for the ground state S_0-(^1A_g) and the excited states $S_1(^1B_{3u})$, $S_2(^1B_{2u})$, $S_3(^1A_u)$, $T_2(^3B_{1u})$, $T_3(^3A_u)$, $T_4(^3B_{2u})$, $T_5(^3B_{2g})$, and $T_6(^3B_{1u})$ of pyrazine evaluated using a selection of SVWN, B3LYP, CIS, SCF, MP2, and CASSCF methodologies. This information is available free of charge via the Internet at http://pubs.acs.org.

References and Notes

(1) Innes, K. K.; Ross, I. G.; Moomaw, W. R. *J. Mol. Spectrosc.* **1988**, *132*, 492.
(2) Del Bene, J. E. *J. Am. Chem. Soc.* **1975**, *112*, 9405.
(3) Del Bene, J. E. *Chem. Phys.* **1976**, *15*, 463.
(4) Wadt, W. R.; Goddard, W. A., III. *J. Am. Chem. Soc.* **1975**, *97*, 2034.
(5) Wadt, W. R.; Goddard, W. A., III; Dunning, T. H. *J. Chem. Phys.* **1976**, *65*, 438.
(6) Kleier, D. A.; Martin, R. L.; Wadt, W. R.; Moomaw, W. R. *J. Am. Chem. Soc.* **1982**, *104*, 60.
(7) Fülscher, M. P.; Andersson, K.; Roos, B. O. *J. Phys. Chem.* **1992**, *96*, 9204.
(8) Foresman, J. B.; Head-Gordon, M.; Pople, J. A.; Frisch, M. J. *J. Phys. Chem.* **1992**, *96*, 135.
(9) Ågren, H.; Knuts, S.; Mikkelsen, K. V.; Jensen, H. J. Aa. *Chem. Phys.* **1992**, *159*, 211.
(10) Woywod, C.; Domcke, W.; Sobolewski, A. L.; Werner, H.-J. *J. Chem. Phys.* **1994**, *100*, 1400.
(11) Stock, G.; Woywod, C.; Domcke, W.; Swinney, T.; Hudson, B. C. *J. Chem. Phys.* **1995**, *100*, 1.
(12) Martin, J. M. L.; Van Alsenoy, C. *J. Phys. Chem.* **1996**, *100*, 6973.
(13) Bauernschmitt, R.; Ahlrichs, R. *Chem. Phys. Lett.* **1996**, *256*, 454.
(14) Del Bene, J. E.; Watts, J. D.; Bartlett, R. J. *J. Chem. Phys.* **1997**, *106*, 6051.
(15) Fischer, G. *Vibronic coupling: The interaction between the electronic and nuclear motions*; Academic Press: London, 1984.
(16) Fischer, G. *Chem. Phys. Lett.* **1981**, *79*, 573.
(17) Fischer, G. *Can. J. Chem.* **1993**, *71*, 1537.

(18) Zalewski, E. F.; McClure, D. S.; Narva, D. L. *J. Chem. Phys.* **1974**, *61*, 2964.
(19) Okuzawa, Y.; Fufii, M.; Ito, M. *Chem. Phys. Lett.* **1990**, *171*, 341.
(20) Hoffmann, R.; Imamura, A.; Hehre, W. J. *J. Am. Chem. Soc.* **1968**, *90*, 1499.
(21) Hopfield, J. J. *Proc. Natl. Acad. Sci. U.S.A.* **1974**, *71*, 3640.
(22) Zeng, J.; Hush, N. S.; Reimers, J. R. *J. Chem. Phys.* **1993**, *99*, 1508.
(23) Zeng, J.; Woywod, C.; Hush, N. S.; Reimers, J. R. *J. Am. Chem. Soc.* **1995**, *117*, 8618.
(24) Zeng, J.; Hush, N. S.; Reimers, J. R. *J. Am. Chem. Soc.* **1996**, *118*, 2059.
(25) Reimers, J. R.; Hush, N. S. *Chem. Phys.* **1996**, *208*, 177.
(26) Creutz, C.; Taube, H. *J. Am. Chem. Soc.* **1969**, *91*, 3988.
(27) Weber, P.; Reimers, J. R. *J. Phys. Chem. A* **1999**, *103*, 9821.
(28) Bauernschmitt, R.; Ahlrichs, R. *J. Chem. Phys.* **1996**, *22*, 9047.
(29) Tomer, J. L.; Holtzclaw, K. W.; Pratt, D. W.; Spangler, L. H. *J. Chem. Phys.* **1988**, *88*, 1528.
(30) Kok, P.; Groenen, E. J. J.; van Amersfoort, P. W.; van der Meer, A. F. G. *J. Chem. Phys.* **1997**, *106*, 2984.
(31) Slater, J. C. *Quantum theory of molecules and solids Vol. 4: The self-consistent field for molecules and solids*; McGraw-Hill: New York, 1974.
(32) Vosko, S. H.; Wilk, L.; Nusair, M. *Can. J. Phys.* **1980**, *58*, 1200.
(33) Becke, A. D. *J. Chem. Phys.* **1993**, *98*, 5648.
(34) Frisch, M. J.; Trucks, G. W.; Schlegel, H. B.; Gill, P. M. W.; Johnson, B. G.; Robb, M. A.; Cheeseman, J. R.; Kieth, T. A.; Petersson, G. A.; Montgomery, J. A.; Raghavachari, K.; Al-Laham, M. A.; Zakrzewski, V. G.; Ortiz, J. V.; Foresman, J. B.; Cioslowski, J.; Stefanov, B. B.; Nanayakkara, A.; Challacombe, M.; Peng, C. Y.; Ayala, P. A.; Chen, W.; Wong, M. W.; Andres, J. L.; Replogle, E. S.; Gomperts, R.; Martin, R. L.; Fox, D. J.; Binkley, J. S.; DeFrees, D. J.; Baker, J.; Stewart, J. J. P.; Head-Gordon, M.; Gonzalez, C.; Pople, J. A. *GAUSSIAN 94*; Gaussian Inc.: Pittsburgh, 1995.
(35) Bauernschmitt, R.; Häser, M.; Treutler, O.; Ahlrichs, R. *Chem. Phys. Lett.* **1997**, *264*, 573.
(36) Ahlrichs, R.; Bär, M.; Baron, H.-P.; Bauernschmitt, R.; Böcker, S.; Ehrig, M.; Eichkorn, K.; Elliot, S.; Haase, F.; Häser, M.; Horn, H.; Huber, C.; Huniar, U.; Kattannek, M.; Kölmel, C.; Kollwitz, M.; Ochsenfeld, C.; Öhm, H.; Schäfer, A.; Schneider, U.; Treutler, O.; von Arnim, M.; Weigend, F.; Weis, P.; Weiss, H. *TURBOMOLE*, Version 4; Quantum Chemistry Group, University of Karlsruhe: Karlsruhe, Germany, 1997.
(37) Fülscher, M. P.; Roos, B. O. *Theor. Chim. Acta* **1994**, *87*, 403.
(38) Foresman, J. B.; Head-Gordon, M.; Pople, J. A.; Frisch, M. J. *J. Phys. Chem.* **1992**, *96*, 135.
(39) Moller, C.; Plesset, M. S. *Phys. Rev. A* **1971**, *46*, 618.
(40) Andersson, K.; Malmqvist, P.-Å.; Roos, B. O. *J. Chem. Phys.* **1992**, *96*, 1218.
(41) Andersson, K.; Blomberg, M. R. A.; Füscher, M. P.; Karlström, G.; Lindh, R.; Malmqvist, P.-Å.; Neogrády, P.; Olsen, J.; Roos, B. O.; Sadlej, A. J.; Seijo, L.; Serrano-Andrés, L.; Siegbahn, P. E. M.; Widmark, P.-O. *MOLCAS*, Version 4; University of Lund: Lund, Sweden.
(42) Helgaker, T.; Jensen, H. J. Aa.; Joergensen, P.; Olsen, J.; Ruud, K.; Aagren, H.; Andersen, T.; Bak, K. L.; Bakken, V.; Christiansen, O.; Dahle, P.; Dalskov, E. K.; Enevoldsen, T.; Fernandez, B.; Heiberg, H.; Hettema, H.; Jonsson, D.; Kirpekar, S.; Kobayashi, R.; Koch, H.; Mikkelsen, K. V.; Norman, P.; Packer, M. J.; Saue, T.; Taylor, P. R.; Vahtras, O. *DALTON*, release 1.0; 1997.
(43) Werner, H.-J.; Knowles, P. J.; Almlöf, J.; Amos, R. D.; Deegan, M. J. O.; Elbert, S. T.; Hampel, C.; Meyer, W.; Peterson, K.; Pitzer, R.; Stone, A. J.; Taylor, P. R.; Lindh, R.; Mura, M. E.; Thorsteinsson, T. *MOLPRO-97 program package*.
(44) The atoms boron through neon and hydrogen: Dunning, T. H., Jr. *J. Chem. Phys.* **1989**, *90*, 1007.
(45) Billes, F.; Mikosch, H. *J. Mol. Struct.* **1995**, *349*, 409.
(46) Wilson, E. B., Jr.; Decius, J. C.; Cross, P. C. *Molecular Vibrations*; McGraw-Hill: New York, 1955.
(47) Walker, I. C.; Palmer, M. H. *Chem. Phys.* **1991**, *153*, 169.
(48) Finley, J.; Malmqvist, P.-Å.; Roos, B. O.; Serrano-Andrés, L. *Chem. Phys. Lett.* **1998**, *288*, 299.
(49) Udagawa, Y.; Ito, M.; Suzuka, I. *Chem. Phys.* **1980**, *46*, 237.
(50) Esherick, P.; Zinsli, P.; El-Sayed, M. A. *Chem. Phys.* **1975**, *10*, 415.
(51) Knoth, I.; Neussor, H. J.; Schlag, E. W. *Z. Naturforsch. A* **1978**, *34*, 979.
(52) Spielfiedel, A.; Handy, N. C. *Phys. Chem. Chem. Phys.* **1999**, *1*, 2401.
(53) McDonald, D. B.; Rice, S. A. *J. Chem. Phys.* **1981**, *74*, 4893.